Appl. Phys. B (2015) 119:133–142
DOI 10.1007/s00340-014-6001-0

Applied Physics B
Lasers and Optics

Remote ambient methane monitoring using fiber-optically coupled optical sensors

Stephen B. Schoonbaert · David R. Tyner · Matthew R. Johnson

Received: 31 October 2014 / Accepted: 29 December 2014 / Published online: 15 January 2015

Abstract A tunable diode laser absorption spectroscopy system, employing a 2*f* wavelength modulation spectroscopy measurement scheme, was developed for remote monitoring of ambient methane fluctuations by way of fiber-optically connected all-optical sensors. Detection of fugitive methane emissions demands a measurement precision less than 2.0 ppm_v and a lower detection limit less than ~1.7 ppm_v methane in air. To determine the optimum base system configuration, the influence of the laser driving signal frequency and amplitude was characterized to strike a balance between measurement precision and system sensitivity. In addition, relative to the basic system configuration, a 50 and 96 % reduction in measurement deviation was achieved by way of polarization scrambling and thermal stabilization of critical optical components, respectively. For methane concentrations between 2.0 and 50.0 ppm_v in air, the laboratory-based system achieved a measured precision of 1.36 ppm_v and a lower detection limit of 1.56 ppm_v using a 6.0-m single-mode optical fiber and an averaging time of 1 s. The long-term system stability and system performance were analyzed using datasets acquired 4 and 12 months after the initial system calibration, yielding a difference in measured precision within the uncertainties of the calibration gas mixture. Finally, it was determined that fiber length between individual remote optical sensors can lead to a varying measurement bias, which implies that length-specific calibrations for each remote optical sensor may be required for a field implementation.

S. B. Schoonbaert · D. R. Tyner · M. R. Johnson (✉)
Energy and Emissions Research Lab, Mechanical and Aerospace Engineering, Carleton University, Ottawa, ON, Canada
e-mail: Matthew_Johnson@carleton.ca

1 Introduction

Fugitive emissions, defined as unintended or irregular leaks of gases and vapors, are an important source of air pollution that is difficult to monitor and control [1]. Within industrial facilities such as oil and gas processing plants, fugitive methane emissions can be a significant source of greenhouse gas emissions [2, 3]. Greenhouse gas data reported by Annex I countries to the United Nations Framework Convention on Climate Change (UNFCCC) suggest that fugitive emissions accounted for ~5 % of global greenhouse gas emissions in 2012 [4]. Detection of fugitive methane is often difficult because the gaseous plumes emanating from individual sources are often intermittent and at low concentrations relative to ambient values of ~1.7 ppm_v [5, 6]. Moreover, current methods for detection of fugitive emissions, which most often involve using survey teams equipped with handheld vapor analyzers [7] or infrared cameras [8], are generally labor-intensive and necessarily intermittent. Recent work on trajectory and inverse methods for interpreting sensor network data to locate and quantify unknown fugitive sources suggests that a measurement standard deviation of 2 ppm_v (equivalent to an absorbance of 8.1×10^{-7} cm^{-1} for the $2\nu_3$ $R(3)$ methane manifold at standard atmospheric pressure and temperatures) is sufficient to locate and potentially quantify fugitive methane sources using statistical methods [9], and possibly as high as 29 ppm_v using adjoint-based inverse dispersion modeling [10].

This paper reports development and quantitative testing of a fiber-coupled, optically networked detection system designed for measuring in situ ambient methane concentrations within an industrial environment, such as an oil and gas processing plant. Quantification of methane at near-ambient concentrations is challenging, and for this

Table 1 Performance characteristics of all-optical fiber-based TDLAS systems

Reference	Publication year	Detection technique†	Conditions of validation‡	Wavelength of calculated*** absorption feature maximum* (nm)	Concentration standard deviation** (1σ) (ppm_v)	Absorbance standard deviation*** (1σ) (cm^{-1})
Chan et al. [14]	1985	DA	1.0 % CH_4 in air	1,665.962	1,315.8[a]	5.2×10^{-4}
Li [15]	2006	2*f*-WMS	790 ppm_v CH_4 in air	1,645.543	750[b]	3.7×10^{-4}
Ho et al. [16]	2000	2*f*-WMS	0.94 % C_2H_2 in air	1,530.371	270[b]	3.2×10^{-4}
Yu et al. [17]	2001	2*f*-WMS	1.0 % C_2H_2 in air	1,530.371	165	1.9×10^{-4}
Zhang et al. [18]	2012	DA	1.0 % CH_4 in air	1,645.543	100	4.9×10^{-5}
Stewartet al. [19]	2010	2*f*-WMS	25 ppm_v CH_4 in air	1,650.959	50[c]	2.4×10^{-5}
Bauer et al. [20]	2014	2*f*-PA	100 ppm_v C_2H_2 in N_2	1,532.831	2.5	2.7×10^{-6}
Tai et al. [21]	1992	2*f*-WMS	350 ppm_v CH_4 in air	1,665.962	5[b]	2.0×10^{-6}
Cao et al. [22]	2013	2*f*-PA	1.0 % C_2H_2 in N_2	1,555.836	4.3	6.7×10^{-9}
He et al. [23]	2014	CRDS	9 ppm_v NH_3 in N_2	1,531.682	0.0216	5.4×10^{-9}

* The calculated wavelength of the most prominent manifold within 0.2 nm of the reported center wavelength

** For the reported species

*** Calculated using the 2012 HITRAN database [13] and Lorentz profiles at 101,325 Pa and 296 K

† *CRDS* cavity ring-down spectroscopy, *DA* direct absorption, *2f-WMS* second-harmonic wavelength modulation spectroscopy, *PA* Photo-acoustic

‡ To the authors' knowledge, all have been validated at ambient pressures and temperatures

[a] Converted from 1 Torr CH_4 in air at 101,325 Pa and 296 K

[b] Calculated using the reported signal-to-noise ratio

[c] Calculated as equal to the "detection threshold"

type of application, measurement accuracy, sensitivity, and response time are critical. After a survey of possible detection methods, tunable diode laser absorption spectroscopy (TDLAS) was selected due to its theoretical ability to meet required performance criteria while possessing other desirable attributes including gas species selectivity, flexible multiplexing options via commonly available optical telecommunications hardware, and the potential for intrinsically safe detection where electricity is not required at each sensor.

Spectroscopic measurement of atmospheric methane is an established technique, but it has not often been extended to remote detection by way of fiber-coupled all-optical sensors. Although high-sensitivity fiber-coupled optoelectric systems have been demonstrated (e.g., [11, 12]), in an industrial environment where intrinsic safety is paramount, systems with remote sensors that do not require detectors or electrically actuated optics are of particular interest. Table 1 summarizes published data for systems that utilize inherently intrinsically safe, all-optical, fiber-coupled sensors for the measurement of gases at atmospheric pressures and temperatures. To compare the performance of spectroscopic systems employing differing hardware topologies and targeting different gas species, concentration measurement deviations are recalculated in terms of a species-independent instrument-specific absorbance in Table 1. For each gas species, calculations were performed using spectral parameters from the 2012 HITRAN database [13], the most prominent manifold within 0.2 nm of the reported center wavelength, and a Lorentzian lineshape at 101.325 kPa and 296 K.

Since Chan et al. [14] presented a fiber-coupled remote optical sensor constructed using microscope lenses for beam collimation, there has been steady improvement in the reported measurement standard deviation for fiber-coupled gas sensors. The most notable detection limits have been reported recently using systems implementing cavity ring-down spectroscopy (CRDS), second-harmonic wavelength modulation spectroscopy (2*f*-WMS), and second-harmonic photo-acoustic spectroscopy (2*f*-PA).

He et al. [23] demonstrated quantification of ammonia in nitrogen with a remote fiber-coupled CRDS-based optical sensor, achieving a measurement deviation (in terms of absorbance) of approximately 5.4×10^{-9} cm^{-1}. Although sensitive and expandable to multiple all-optical sensors, the CRDS method requires high-quality mirrors and precise optical alignment to achieve the best measurement performance, necessitating compromises between sensitivity and sensor cost.

Bauer et al. [20] demonstrated detection of acetylene in nitrogen using 2*f*-PA spectroscopy via a low-cost 3-D-printed sensor (with integrated microphone), in which

an absorbance precision of 2.7×10^{-6} cm^{-1} was calculated based on measurements of 100 ppm$_v$ acetylene in nitrogen. Similarly, Cao et al. [22] demonstrated an all-optical 2*f*-PA-based system, achieving an absorbance precision of 6.7×10^{-9} cm^{-1} acetylene in nitrogen. Even though these are promising advancements in remote optical 2*f*-PA indicating the viability of low-cost sensor solutions, the fragility of the diaphragm, sensitivity to external acoustic and vibrational noise [24], and its reliance on diffusion through micro-channels could limit its compatibility with detection of ambient methane in an industrial environment.

Stewart et al. [19] demonstrated the potential of 2*f*-WMS-based remote multi-point open-path detection of methane in industrial environments, reporting on various iterations where performance was limited by optical fringes, noise, and system drift [25, 26]. Tai et al. [21] presented a fiber-coupled continuous-wave 2*f*-WMS-based system capable of achieving a minimum drift-limited detectable absorbance of 2.0×10^{-6} cm^{-1} estimated from results obtained with an optically simplistic 10-cm fiber-coupled interrogation cell containing 350 ppm$_v$ methane in nitrogen. The simplicity, selectivity, and theoretically achievable precision of the 2*f*-WMS technique show promise for remote monitoring of ambient methane, but will require specific attention to system design to achieve a measurement precision and lower detection limit required for detecting and monitoring fugitive methane plumes [9], less than 8.1×10^{-7} and 6.9×10^{-7} cm^{-1}, respectively.

In the present work, a purpose-built TDLAS system with the ability to optically monitor ambient methane over multiple multiplexed sensors via a telecommunications-grade single-mode (SM) fiber-optical network is presented. The test system was modularly designed to enable quantitative comparison of various hardware and software changes to reach the desired system measurement performance characteristics.

2 Methodology/apparatus

The present TDLAS system employs all-fiber optical routing for robustness and compactness and includes fiber-coupled components such as the tunable diode laser, reference gas cell, and fiber-ring resonator. A schematic of the complete system, consisting of the base TDLAS system and fiber-coupled remote optical sensor, is provided in Fig. 1.

The requirement to detect low concentrations of methane at ambient pressures and temperatures using an array of sensors governed the design of the remote optical sensors. The custom fiber-coupled open-path optical sensors employ an arrangement of planar reflective surfaces that route the laser beam through an open interrogation region, achieving a total optical path length of 5.79 m in 8 passes. The laser beam is coupled in and out of the interrogation region using a wavelength-optimized fiber-coupled aspheric lens collimator with optical routing facilitated by way of a three-port optical circulator.

The fibers used within this system are telecommunications-grade single-mode (SM) optical fibers. Within the base TDLAS system, 900-µm loose-tube fibers were used, as flexibility was more critical than durability. Reinforced jacketed fibers were used to couple the remote optical sensor to the base station, identical to what would be used when deployed in the field. Where physical fiber connections were required, high-polish FC/APC-type connectors were used to minimize back-reflections and unwanted optical interference. SM fibers were selected over polarization-maintaining fibers due to their lower cost and higher bandwidth. The laser in this setup is an InGaAs fiber-coupled distributed feedback (DFB) diode (NEL, NLK1U5EAAA), with an approximate spectral linewidth of 2.0 MHz and a fiber output power of approximately 15 mW. This diode was spectrally tuned to the near-infrared $2\nu_3 R(3)$ methane manifold located near 1,653.73 nm at atmospheric temperatures and pressures.

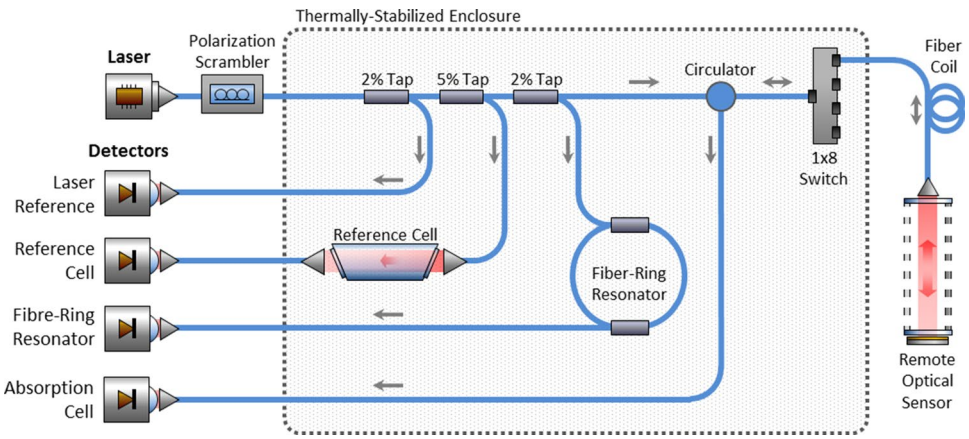

Fig. 1 Schematic of the base TDLAS system and remote fiber-coupled optical open-path sensor

The reference cell is a fixed-volume interrogation cell containing 5.0 % methane in nitrogen at atmospheric pressure, which provides an easily distinguished signal onto which the TDLAS system can lock on for the purposes of system calibration and counteracting wavelength drift. A fiber-ring resonator (FRR) is tapped directly off the laser, providing a means of accurately quantifying the time-varying wavelength by way of optical interference fringes, with similar functionality to a free-space etalon.

The single-mode fibers, and in particular the fiber-based optical components used in this system, are sensitive to polarization-dependent loss and dispersion, which in turn is influenced by ambient temperature. Polarization scramblers are commonly used in optical communication systems to reduce polarization-dependent effects by introducing a random polarization within the fiber network. The result of polarization scrambling is an increase in the instantaneous intensity variation, fluctuating about a common mean. When time-averaged, the degree of polarization of the resultant signal approaches zero, resulting in a reduced perceived intensity variation. The potential utility of a General Photonics polarization scrambler (PCD-104, implementing a multiple-stage birefringent modulator via four piezoelectric transducers) was tested for mitigating the influence of polarization variation on methane volume mixing ratio measurements.

To stabilize the optical system, the optical components most susceptible to temperature fluctuations (taps, couplers, circulator, optical attenuators, FRR, reference cell, and optical relay) are housed within an insulated enclosure. The temperature within the enclosure is stabilized to within 0.1 °C using a thermoelectric heating and cooling system. To ensure efficient heat transfer, the optical components are mounted to a polished aluminum plate which is bonded to the Peltier element of the heating/cooling system.

A gas mixing system comprised of two mass-flow controllers was used to calibrate and assess system performance. Varying concentrations of methane were created by mixing compressed air or bottled calibration-grade nitrogen with premixed calibration gas (2.00 ± 0.02 % methane in nitrogen). The gas mixture was then passed through an unpressurized test chamber containing the fiber-coupled remote optical sensor. The uncertainty in the test chamber methane volume mixing ratio, separately confirmed using a MKS Multi-Scan 2030 FTIR gas analyzer, linearly increased from 0.56 to 1.82 ppm_v as the requested methane concentration increased from 2.0 to 50.0 ppm_v.

The TDLAS system synchronously acquires 2*f*-WMS signals from the remote optical sensor and the reference cell, which are spectrally centered on the $2\nu_3$ *R*(3) methane manifold. Due to the potentially low signal-to-noise ratio of the remote optical cell second-harmonic signal during measurements at low methane concentrations, the reference cell 2*f* signal maximum is used to provide the time index at which the absorption manifold peak is traversed, and is subsequently used to infer a 2*f* value from the remote optical sensor signal as illustrated in Fig. 2. The measured remote optical sensor 2*f* signal is then converted to a methane volume mixing ratio using either a theoretical or an experimental calibration as further detailed below.

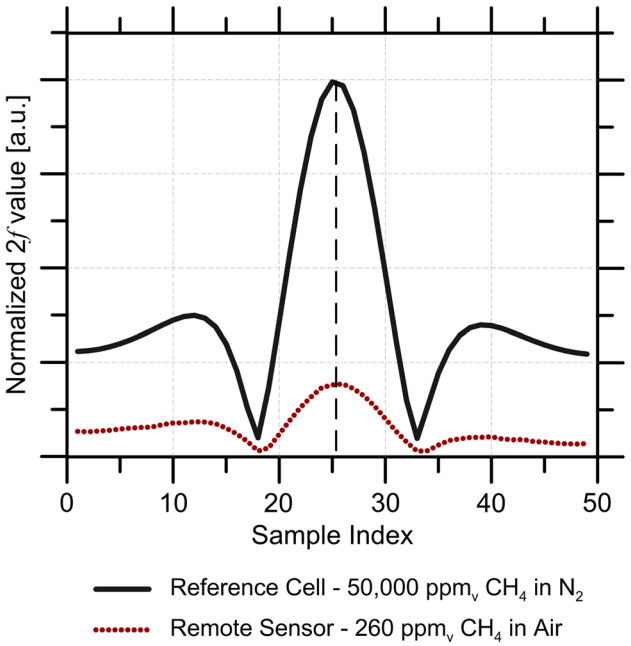

Fig. 2 Inferred remote optical cell 2*f* value from reference cell 2*f* signal maximum

2.1 Theoretical calibration

To investigate the utility of a calibration based on spectroscopy theory, a lookup table was pre-calculated using theoretical 2*f*-WMS signals and methane spectral parameters from HITRAN [27]. The theoretical signals used to generate the lookup table were generated following the procedures found in [28, 29], as further explained here. The pressure, *P* (Pa), and temperature, *T* (K), range covered by the table encompasses what is normally observed in the laboratory, and the overall resolution of the table is balanced to offset the interpolation time of a single value. The instantaneous wave number and absorption-free intensity of the laser output, $\nu(t)$ (cm^{-1}) and $I_0(t)$ (V), follow:

$$I_0(t) = \bar{I}_0(1 + i_0 \cos(2\pi ft + \psi_1) + i_2 \cos(4\pi ft + \psi_2)), \quad (1)$$

$$\nu(t) = \bar{\nu} + a \cos(2\pi ft), \quad (2)$$

where $\bar{I}_o$ and $\overline{V}$ are the mean absorption-free intensity (V) and associated center wave number (cm^{-1}) over the modulation period, *f* is the modulation frequency (s^{-1}), *a* is the

spectral modulation depth (cm^{-1}), and i_0 and i_2 are the first- and second-order modulation intensity amplitudes (V) at f and $2f$, respectively. Additionally, ψ_1 and ψ_2 account for the phase shifts between the first- and second-order modulation intensity and wavelength signals. The post-absorption intensity signal, $I(t)$, is modeled with the Beer–Lambert–Bouger Law, evaluated at $\nu(t)$, and the laser intensity absorption-free intensity, $I_0(t)$, using

$$I(t) = I_0(t) \exp\left(-\frac{qPL}{kT}\sigma(\nu(t))\right), \tag{3}$$

where k is Boltzmann's constant [1.380658 $\times$ 10^{-19} (kg cm^2)/(s^2 K)], q is the volume mixing ratio, L is the optical path length (m), and σ is the absorption cross section (cm^2/molecule) defined by the product of absorption line strength and lineshape. For this application, a Lorentz lineshape was chosen to reduce table pre-computation time. The difference in estimated second-harmonic, $2f$, values for Lorentz and a Voigt profiles is negligible when using the calibration described in Sect. 3.2.

The transmittance, and subsequent absorption, can be written in terms of a Fourier series (with coefficients H_c) with reference to only the high-frequency modulation component of the laser injection signal. To simplify notation, let $\eta = 2\pi ft$. The transmittance can be written as

$$\frac{I(t)}{I_0(t)} = \tau(\nu(t)) = \sum_{c=0}^{\infty} H_c(\bar{\nu}, a)\cos(c\eta). \tag{4}$$

From this, the Fourier coefficients are defined by,

$$H_0(\bar{\nu}, a) = \frac{1}{2\pi}\int_{-\pi}^{\pi} \tau(\bar{\nu} + a\cos(\eta))d\eta, \text{ and} \tag{5}$$

$$H_c(\bar{\nu}, a) = \frac{1}{\pi}\int_{-\pi}^{\pi} \tau(\bar{\nu} + a\cos(\eta))\cos(c\eta)d\eta, c \in \mathbb{N}\backslash\{0\}. \tag{6}$$

The second-harmonic, $2f$, signal can be obtained by summing the even and odd second-harmonic terms and computing the root sum square,

$$R_{2f} = \sqrt{X_{2f}^2 + Y_{2f}^2}, \tag{7}$$

where

$$\begin{aligned} X_{2f} &= \frac{1}{2\pi}\int_{-\pi}^{\pi} I_0(t)\tau(\nu(t))\cos(2\eta)d\eta \\ &= \frac{\bar{I}_o}{2}\left(H_2 + \frac{i_0}{2}(H_1 + H_3)\cos(\psi_1) + i_2\left(H_0 + \frac{H_4}{2}\right)\cos(\psi_2)\right) \end{aligned} \tag{8}$$

and

$$\begin{aligned} Y_{2f} &= \frac{1}{2\pi}\int_{-\pi}^{\pi} I_0(t)\tau(\nu(t))\sin(2\eta)d\eta \\ &= -\frac{\bar{I}_o}{2}\left(\frac{i_0}{2}(H_1 - H_3)\sin(\psi_1) + i_2\left(H_0 - \frac{H_4}{2}\right)\sin(\psi_2)\right). \end{aligned} \tag{9}$$

To permit real-time compensation for return intensity fluctuations, the lookup table includes the first five Fourier coefficients $\{H_0,\ldots, H_4\}$, computed at the wavelength of the theoretical $2f$ feature maximum. The theoretical $2f$ value, R_{2f}, is then recomputed using the estimated absorption-free intensity and known laser intensity and wavelength response characteristics ($\bar{I}_0$, i_0, i_2, ψ_1, ψ_2). The resultant calibration function

$$\widehat{q} = G\left(\mathrm{LUT}_{\mathrm{WMS}}\left(x_{2f}, T_{\mathrm{amb}}, P_{\mathrm{amb}}\right) - b\right), \tag{10}$$

permits the transformation of measured $2f$ values, x_{2f}, to a methane volume mixing ratio, $\widehat{q}$, described by the WMS theoretical lookup table, $\mathrm{LUT}_{\mathrm{WMS}}$, and calibration coefficients, G and b (commonly referred to as the calibration factor, G, and the zero response, respectively). These calibration coefficients are determined once during system commissioning by fitting a linear calibration function to the theoretical lookup table result relative to the requested test chamber methane volume mixing ratio.

2.2 Experimental calibration

Unlike the theoretical calibration, the experimental calibration used here depends only on the measured $2f$ values, x_{2f}, and mean return intensity from the remote optical cell, I, and follows a constrained fourth-order polynomial,

$$\begin{aligned} \widehat{q} &= \mathrm{CAL}_{\mathrm{WMS}}\left(x_{2f}, I\right) \\ &= x_{2f}\left(G_3I^3 + G_2I^2 + G_1I + G_0\right) + G_4I^3 + G_5I^2 + G_6I + G_7 \end{aligned} \tag{11}$$

This function permits the transformation of measured $2f$ values to a methane volume mixing ratio, without the inclusion of ambient pressure and temperature or the laser response characteristics. It should be noted that the dataset used to determine the polynomial coefficients, $\{G_0,\ldots, G_7\}$, must include the temperature, pressure, and intensity variations over which the function is intended to be used. For this system, the lack of any return intensity controllability necessitated the acquisition of calibration data over the course of multiple days.

3 Results

The optimum laser input signal frequencies and amplitudes for the WMS technique are often stated when the $2f$ signal is maximized [29–32]. However, for this system, the optimum

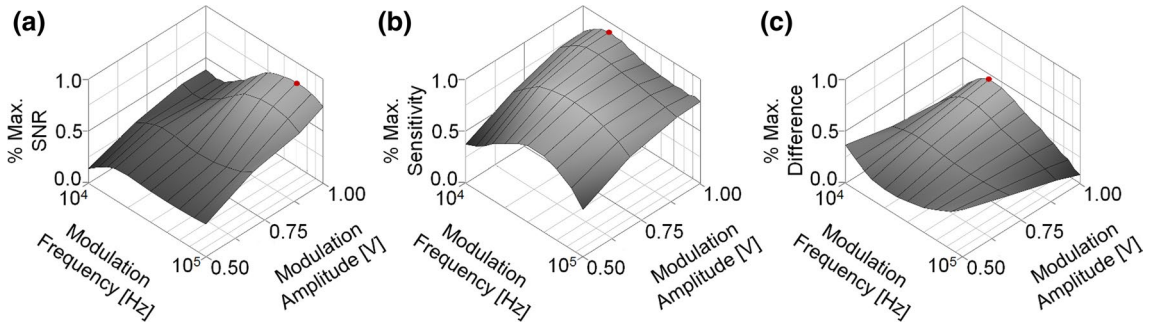

Fig. 3 Optimization parameter results for theoretical methane volume mixing ratios at 10 ppm_v methane in air: **a** 2*f* SNR, **b** 2*f* calibration sensitivity, **c** difference between the theoretical and experimental 2*f* values

is a combined function of the experimentally measured 2*f* signal-to-noise ratio, the 2*f* value sensitivity (the change in the measured absorption or 2*f* peak height for a given change in test chamber methane volume mixing ratio ($\Delta x_{2f}/\Delta q$)), and the absolute difference between the experimental and theoretical 2*f* peak ($1 - \left|\left(x_{2f} - R_{2f}\right)/x_{2f}\right|$). The optimum laser input signal was assessed within the constraints of the system. The maximum and minimum frequencies are constrained by the data acquisition hardware (100 kHz, limited by the digitizer sample rate of 2 MHz and the constraint of having sufficient sample points to precisely resolve the 2*f* signal) and laser controller stability (10 kHz), respectively, whereas the maximum amplitude is constrained by the laser diode (1.0 V, corresponding to 20 mA). Figure 3 illustrates the summed non-dimensional results for these three optimization parameters at a requested methane concentration of 10 ppm_v in air (at 101.325 kPa and 296 K), with the most desirable frequency and amplitude indicated at the surface maximum.

The maximum 2*f* feature value occurs at a modulation frequency of 80 kHz and modulation amplitude of 1.0 V. The maximum change in the measured 2*f* value with a change in requested volume mixing ratio occurs at lower frequencies and higher amplitudes, 20 kHz and 1.0 V. The experimentally measured 2*f* value matches theoretical estimations most closely at low sweep amplitudes and frequencies, 0.5 V and 20 kHz, respectively. The equally weighted sum of the normalized parameters at a requested methane concentration of 10 ppm_v yields an optimum laser input signal frequency and amplitude at a low laser injection modulation frequencies and high modulation amplitudes, as illustrated in Fig. 4.

The resultant optimum occurs at the minimum modulation frequency and maximum modulation amplitude constrained by the available system hardware, 10 kHz and 1.0 V, respectively, consistent with results obtained at methane volume mixing ratios between 2.0 and 50 ppm_v. In the experiments presented below, an optimum wavelength sweep frequency of 100 Hz and amplitude of

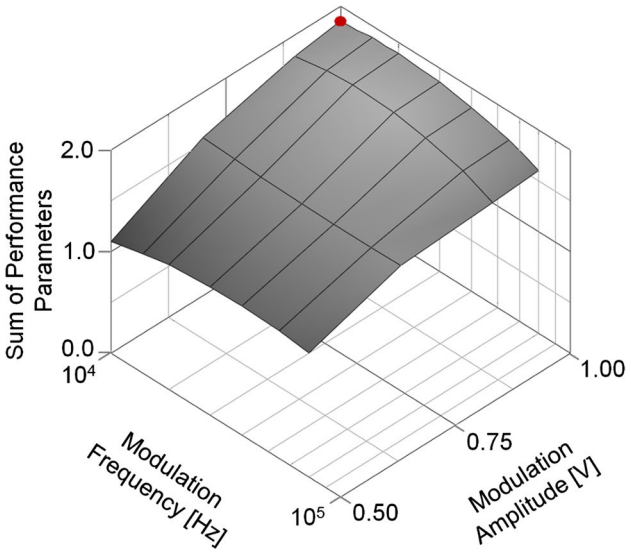

Fig. 4 Optimum modulation frequency and amplitude (maximum) for achievable laser input signal modulation frequencies and amplitudes

75 mV were used, which balances the trade-offs between 2*f* feature resolution, measurement rate, and signal generation limitations.

3.1 Drift compensation

The effects of polarization scrambling and thermal stabilization on measured 2*f* value deviation using the aforementioned optimum laser driving signals are illustrated in the Allan–Werle deviation plot in Fig. 5. This plot demonstrates measured remote optical sensor 2*f* value deviation (2σ) using the 5.79-m optical sensor within a nitrogen-purged test chamber near STP, coupled to the base system with a 6.0-m SM optical fiber. The thermal enclosure was maintained at a constant 21.10 °C when activated, maximizing the second-harmonic signal sensitivity to changes in methane volume mixing ratio within the fiber-coupled

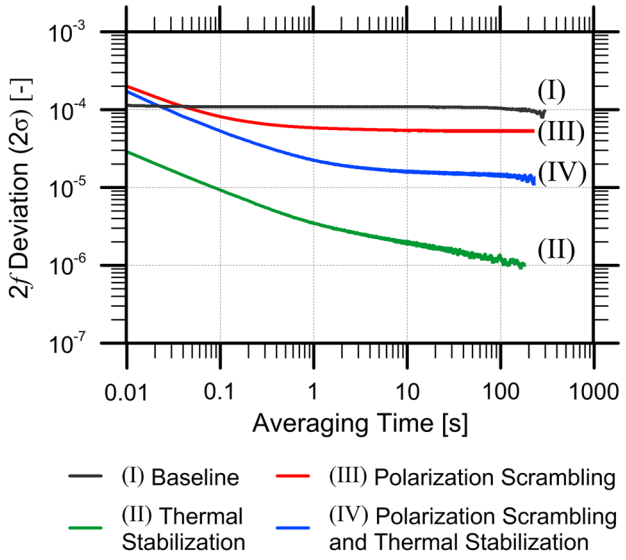

Fig. 5 Allan–Werle deviation plot of measurement deviation reduction by thermal stabilization and polarization scrambling

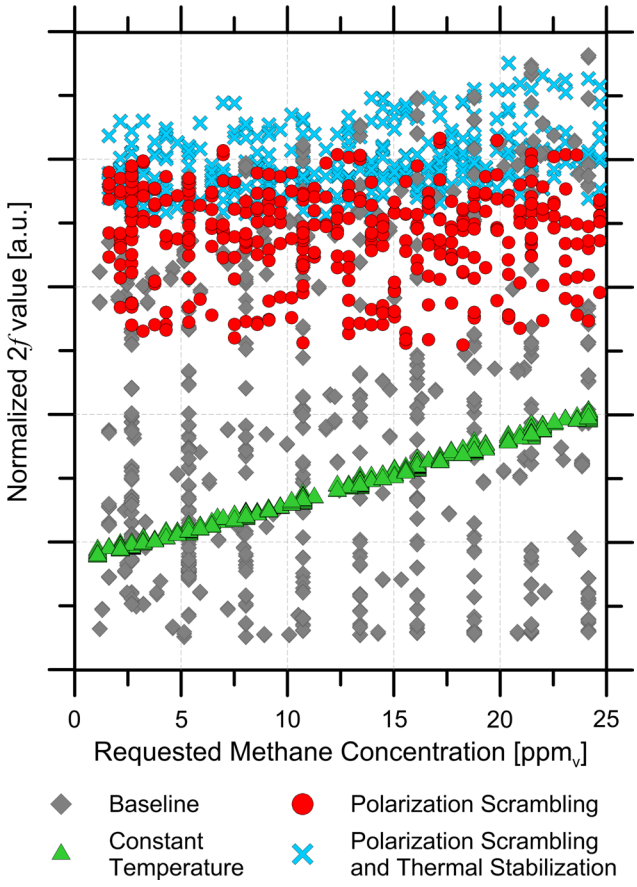

Fig. 6 One-second-averaged normalized 2*f* measurements (using the 5.79-m fiber-coupled remote optical sensor) for various methods of system drift suppression

optical sensor, and ensuring efficiency and stability of the thermal control system.

When compared to the baseline case, the addition of the polarization scrambler, as expected, increased the instantaneously measured *2f* value deviation, but reduced the measurement deviation by greater than 50 % with averaging times greater than 1.0 s. Thermal stabilization with no polarization scrambling yielded the lowest measurement standard deviation, which was consistently at least an order of magnitude lower than that achieved with the polarization scrambler, for averaging times greater than 0.5 s. Interestingly, the positive effects of thermal stabilization on the measured 2*f* value deviation are reduced when combined with polarization scrambling. This may be attributable to the piezoelectric transducers internal to the polarization scrambler that impart polarization and amplitude modulation at four fixed frequencies (each less than 700 kHz). This in turn would influence the measured signal deviation at the sweep and modulation frequencies of 100 Hz and 20 kHz, which may not be fully suppressed with signal averaging.

Even though long averaging times yielded the lowest signal deviation, these times are not useful for the intended application of observing transient ambient methane plumes, or in a case where sensors are multiplexed and sequentially interrogated. Averaging optical measurements for 1 s balances the trade-offs between minimizing measurement duration and increasing measurement precision by reducing random scatter.

To illustrate typical measurement deviation and scatter, Fig. 6 shows normalized remote interrogation cell 2*f* values for system configurations with and without thermal stabilization and polarization scrambling. The displayed 1-s-averaged results were acquired at requested test chamber methane volume mixing ratios between 2.0 and 25.0 ppm_v at pressures between 98 and 103 kPa, and temperatures between 21 and 27 °C. The tests were conducted with the remote optical sensor connected to the base TDLAS system via a 6.0-m SM optical fiber.

3.2 Calibration results

The system calibration functions were determined following the ISO 9169 standard as described by Werle et al. [33]. The calibration dataset spans 2.0–100 ppm_v methane in air, with at least 10 repeated measurements at greater than 25 requested concentrations. Unique calibration coefficients can be used to describe the theoretical and experimental calibration functions with confirmed negligible non-linearity. The calibration dataset consists of measured remote optical sensor 2*f* values averaged for 1 s, acquired at ambient pressures between 98 and 103 kPa, ambient temperatures between 21 and 25 °C, a thermal enclosure temperature of 20.1 °C, with no polarization scrambler

Table 2 Measurement performance of thermal-stabilized system

Parameter	Calibration method	
	Theoretical	Experimental
Precision (2σ)* (ppm_v)	1.36	1.71
LDL (ppm_v) (95 % prediction interval at $q = 0$)	1.56	2.54
LOD (ppm_v) (95 % confidence interval at $q = 0$)	0.30	0.96

* Quoted as the largest precision value over the tested operating range of 2–50 ppm_v

present, and with the fiber-coupled optical sensor connected to the base TDLAS system with a 6.0-m SM optical fiber.

The measurement precision and lower detection limit (LDL) were determined following Werle et al. [33], and the limit of detection (LOD) was computed following Loock and Wentzell [34]. The LDL is calculated based on the prediction interval of the calibration function at 95 % confidence. The LDL is defined such that the lower bound of the prediction interval at the LDL is equal to the upper bound of the prediction interval at a requested concentration of 0 ppm_v. The LOD is computed in a similar fashion using a 95 % confidence interval. Table 2 lists the maximum measured precision over the intended system operational range (2.0–50.0 ppm_v) and the calculated LDL and LOD with 95 % confidence.

Comparing the two calibration methods for measurements averaged over 1 s, the theoretical calibration yields a 20 % improvement in precision and a 38.5 % decrease in the LDL. The achieved LDL of 1.56 ppm_v (or an instrument-dependent absorbance of 6.32×10^{-7} cm^{-1}) is lower than the targeted LDL of ~1.7 ppm_v (or ~6.9×10^{-7} cm^{-1}) for remote detection of ambient methane. In addition, the obtained measurement precision of 1.36 ppm_v (or 5.51×10^{-7} cm^{-1}) is comparable to the suggested minimum precision of 2.0 ppm_v (or 8.10×10^{-7} cm^{-1}) required to locate fugitive methane sources using statistical trajectory methods [9].

4 Discussion

The long-term stability of system performance was assessed using subsequent datasets acquired 4 and 12 months after the initial calibration. Figure 7 illustrates the measured precision and bias (calculated as the absolute difference between the measured and requested methane concentration) at methane in air concentrations of 2.0 and 50.0 ppm_v.

The results in Fig. 7 illustrate a minimal variation in measurement precision and an increase in measured bias

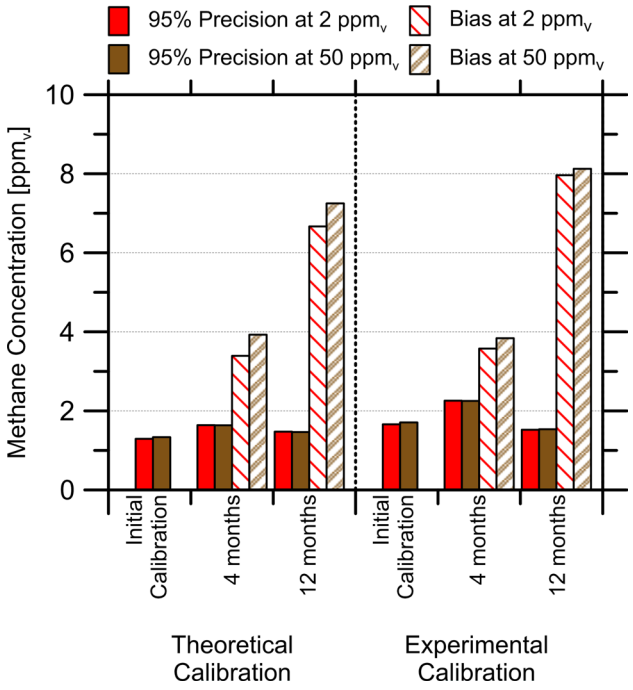

Fig. 7 Long-term system performance results with a 6.0-m optical fiber

to as high as 8.1 ppm_v over the course of a year. The bias increase may be attributable to network fiber replacement between the remote optical sensor and base TDLAS system, as well as the cleaning and realignment of the reflective surfaces within the remote optical sensor. Given that the latter activities would most likely occur during field maintenance and there is also potential for fiber breakage and replacement in an industrial setting, the ambient methane concentration (zero response) would need to be established regularly to minimize the accumulation of bias errors. Simulation suggests [9] that an ambient methane concentration estimation should be achievable by way of software analysis, due to the infrequent interaction of fugitive emission plumes with sensors in a distributed network.

When deployed around an industrial facility, the remote optical sensors could require placement up to 1 km away from the base TDLAS system. To determine the effect of optical fiber length on measured $2f$ values, laboratory tests were conducted with 25-, 100-, and 1,000-m SM fibers added between the interrogation cell and base TDLAS system. The addition of the fibers was the only difference in the otherwise identical hardware, operating, and ambient conditions for the original calibration set. Figure 8 illustrates the measured precision and bias at 2.0 and 25.0 ppm_v, for the fiber lengths tested.

The measurement precision remained relatively consistent among the tested fiber lengths and calibration methods, varying by only slightly more than the methane volume

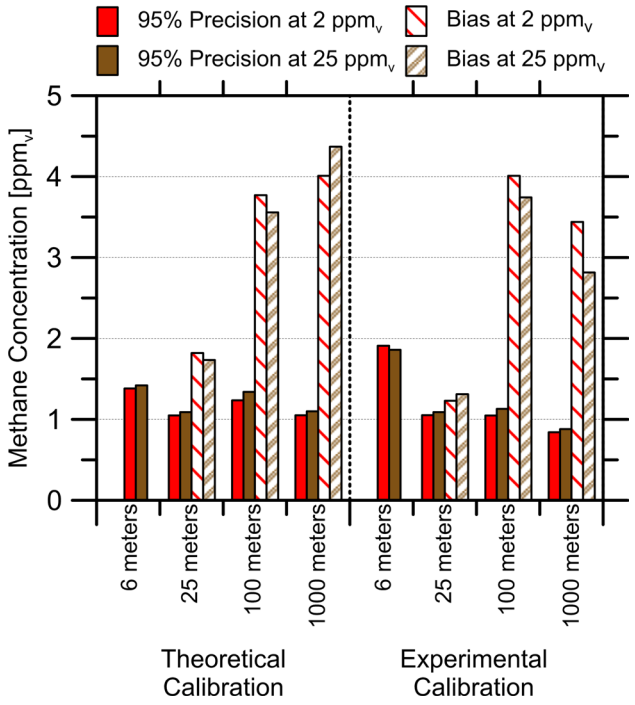

Fig. 8 Effect of SM fiber length on measurement performance

mixing ratio uncertainty from the gas mixing system. The increase in measured bias with increased fiber length suggests fiber length should remain fixed after system commissioning in which the initial calibration could be easily accomplished using lengths specific to the installation or, perhaps more simply, using longer fibers to accommodate varying optical network configurations, with excess fiber coiled where it is safe and convenient.

Based on the superior measurement precision and bias obtained, as listed in Table 2, the theoretical calibration method is more suitable than the experimental calibration method for this application. In addition, knowledge of the ambient temperature and pressure could be made readily available from a single atmospheric monitoring station within the extents of the network, making the theoretical calibration procedures comparatively less complex than the experimental calibration.

Long-term implementation of a fiber-coupled open-path optical sensor in the field presents significant albeit surmountable challenges [19]. Firstly, contamination of the laser beam-steering surfaces can be minimized by enclosing them within a dust and moisture resistant enclosure and passing the laser beam through angled windows coated to ensure high transmittance and resistance to scratches, moisture, and dust buildup. Aside from requiring routine cleaning, signal loss due to window contamination is inherently included in the intensity-normalized calibration and will lead to an increase in the measurement deviation proportional to the decrease in the SNR of the measured 2*f* value.

5 Conclusions

The presented laboratory-based TDLAS system for measuring in situ ambient methane concentrations achieved an average measurement precision of 1.36 ppm_v over optical fiber lengths up to 1 km, and a LDL of 1.56 ppm_v, at an averaging time of 1 s using a theory-based calibration. When compared in terms of an instrument-dependent absorbance, the measured precision (5.51×10^{-7} cm^{-1}) and LDL (6.32×10^{-7} cm^{-1}) values are lower than published results from comparable fiber-coupled 2*f*-WMS systems implementing all-optical remote sensors [19, 21] and meet the suggested requirements for the reliable measurement of transient fugitive methane plumes [9].

The modular nature of the system's fiber components facilitated a study on the effectiveness of reducing measurement scatter by way of a polarization scrambler and thermal control system. Relative to the baseline system, the thermal stabilization of system-critical optical components (e.g., taps, optical switch, fiber-ring resonator, reference cell, etc.) significantly reduced measurement scatter on a 1-s measurement by at least 96 %. This is greater than the decrease in the measured precision achieved using the polarization scrambler alone (54 %) or using the polarization scrambler in combination with thermally stabilized components (80 %). Once thermally stabilized, long-term stability tests and varying fiber lengths (for the theoretical and experimental system calibrations) yielded comparable measurement precision and bias. However, the theoretical calibration would likely be favorable because it is substantially less laborious to implement. Although long-term stability tests showed a marked increase in measurement bias, for the intended application of detection of intermittent fugitive methane plumes this bias could be software-corrected by monitoring background methane concentrations and adjusting the bias accordingly. Additionally, to minimize bias uncertainties, the system should be implemented with calibrations specific to the length of fiber between each remote optical sensor and the base TDLAS components. By surpassing relevant precision and LDL targets for quantifying fugitive methane plumes at near-ambient concentrations, the fiber-optically networked TDLAS system presented here has demonstrated potential for use in the detection of fugitive emissions while using all-optical (intrinsically safe) passive sensors.

References

1. E.P.A. Us, *VOC fugitive losses: new monitors, emission losses, and potential policy gaps* (United States Environmental Protection Agency (US EPA), Washington, D.C., 2006), p. 303
2. D.A. Kirchgessner, R.A. Lott, R.M. Cowgill, M.R. Harrison, T.M. Shires, Chemosphere **35**, 1365 (1997)
3. A.K. Chambers, M. Strosher, T. Wootton, J. Moncrieff, P. McCready, J. Air Waste Manag. Assoc. **58**, 1047 (2008)
4. UNFCCC. http://unfccc.int/ghg_data/ghg_data_unfccc/items/4146.php. Accessed 27 October 2014 (2014)
5. CAPP, *Best management practice: management of fugitive emissions at upstream oil and gas facilities* (Canadian Association of Petroleum Producers (CAPP), Calgary, AB, 2007)
6. J.N. Carras, P.M. Franklin, Y. Hu, A.K. Singh, O.V. Tailakov, D. Picard, F.M.A. Azhari, E. Gjerald, S. Nordrum, I. Yesserkepova, in *2006 IPCC Guildelines Natl. Greenh. Gas Invent. Vol. 2 Energy*, ed. by S. Eggleston, L. Buendia, K. Miwa, T. Mgara, K. Tanabe (Intergovernmental Panel on Climate Change (IPCC), Hayama Japan, 2006), pp. 4.1–4.78
7. US EPA, *Method 21—determination of volatile organic compound leaks* (n.d.), pp. 4–10
8. E.P.A. Us, *Alternative work practice to detect leaks from equipment* (United States Environmental Protection Agency (US EPA), Washington, D.C., 2008)
9. C.A. Brereton, M.R. Johnson, Atmos. Environ. **51**, 46 (2012)
10. I.M. Joynes, *Proof-of-concept inverse micro-scale dispersion modelling for fugitive emissions quantification in industrial facilities* (Carleton University, Ottawa, 2013)
11. B.J. Orr, Y. He, Chem. Phys. Lett. **512**, 1 (2011)
12. Y. He, R. Kan, F.V. Englich, W. Liu, B.J. Orr, Opt. Express **18**, 20059 (2010)
13. L.S. Rothman, I.E. Gordon, Y. Babikov, A. Barbe, D. Chris Benner, P.F. Bernath, M. Birk, L. Bizzocchi, V. Boudon, L.R. Brown, A. Campargue, K. Chance, E.A. Cohen, L.H. Coudert, V.M. Devi, B.J. Drouin, A. Fayt, J.-M. Flaud, R.R. Gamache, J.J. Harrison, J.-M. Hartmann, C. Hill, J.T. Hodges, D. Jacquemart, A. Jolly, J. Lamouroux, R.J. Le Roy, G. Li, D.A. Long, O.M. Lyulin, C.J. Mackie, S.T. Massie, S. Mikhailenko, H.S.P. Müller, O.V. Naumenko, A.V. Nikitin, J. Orphal, V. Perevalov, A. Perrin, E.R. Polovtseva, C. Richard, M.A.H. Smith, E. Starikova, K. Sung, S. Tashkun, J. Tennyson, G.C. Toon, V.G. Tyuterev, G. Wagner, J. Quant. Spectrosc. Radiat. Transf. **130**, 4 (2013)
14. K. Chan, H. Ito, H. Inaba, T. Furuya, Appl. Phys. B **38**, 11 (1985)
15. S. Li, Optical fiber gas sensor for remote detection of methane gas in coal mines, Ph.D. Thesis, Stevens Institute of Technology (2006)
16. H.L. Ho, W. Jin, H.B. Yu, K.C. Chan, C.C. Chan, M.S. Demokan, IEEE Photonics Technol. Lett. **12**, 1546 (2000)
17. H.B. Yu, W. Jin, H.L. Ho, K.C. Chan, C.C. Chan, M.S. Demokan, G. Stewart, B. Culshaw, Y.B. Liao, Appl. Opt. **40**, 1011 (2001)
18. T. Zhang, W. Wang, L. Gao, T. Koscica, and D. Li, in *Proceeding of SPIE 8417, 6th Int. Symp. Adv. Opt. Manuf. Test. Technol. Opt. Test Meas. Technol. Equip*. (2012), pp. 1–6
19. G. Stewart, W. Johnstone, G. Thursby, B. Culshaw, in *Proceeding of SPIE 7675, Photonics Transp. Ind. Auto to Aerosp. III*, ed by A.A. Kazemi, B.C. Kress, E.Y. Chan (Orlando, FL, 2010), pp. 1–9
20. R. Bauer, G. Stewart, W. Johnstone, E. Boyd, M. Lengden, Opt. Lett. **39**, 4796 (2014)
21. H. Tai, K. Yamamoto, M. Uchida, S. Osawa, K. Uehara, IEEE Photonics Technol. Lett. **4**, 804 (1992)
22. Y. Cao, W. Jin, H.L. Ho, J. Ma, Opt. Lett. **38**, 434 (2013)
23. Y. He, C. Jin, R. Kan, J. Liu, W. Liu, J. Hill, I.M. Jamie, B.J. Orr, Opt. Express **22**, 13170 (2014)
24. J. Ye, L.-S. Ma, J.L. Hall, J. Opt. Soc. Am. B **15**, 6 (1998)
25. G. Whitenett, G. Stewart, K. Atherton, B. Culshaw, W. Johnstone, J. Opt. A: Pure Appl. Opt. **5**, S140 (2003)
26. G. Stewart, C. Tandy, D. Moodie, M.A. Morante, F. Dong, Sensors Actuators B Chem. **51**, 227 (1998)
27. L.S. Rothman, I.E. Gordon, A. Barbe, D.C. Benner, P.F. Bernath, M. Birk, V. Boudon, L.R. Brown, A. Campargue, J.-P. Champion, J. Quant. Spectrosc. Radiat. Transf. **110**, 533 (2009)
28. H. Li, G.B. Rieker, X. Liu, J.B. Jeffries, R.K. Hanson, Appl. Opt. **45**, 1052 (2006)
29. G.B. Rieker, J.B. Jeffries, R.K. Hanson, Appl. Opt. **48**, 5546 (2009)
30. P. Chambers, E.A.D. Austin, J.P. Dakin, Meas. Sci. Tech. **15**, 1629 (2004)
31. J.T.C. Liu, J.B. Jeffries, R.K. Hanson, Appl. Opt. **43**, 6500 (2004)
32. S. Schilt, L. Thévenaz, P. Robert, Appl. Opt. **42**, 6728 (2003)
33. P. Werle, P. Mazzinghi, F. D'Amato, M. De Rosa, K. Maurer, F. Slemr, Spectrochim. Acta. A Mol. Biomol. Spectrosc. **60**, 1685 (2004)
34. H.-P. Loock, P.D. Wentzell, Sensors Actuators B Chem. **173**, 157 (2012)